Journal of Power Sources 374 (2018) 257–268

Contents lists available at ScienceDirect

Journal of Power Sources

journal homepage: www.elsevier.com/locate/jpowsour

Isothermal calorimeter for measurements of time-dependent heat generation rate in individual supercapacitor electrodes

Obaidallah Munteshari[a,b], Jonathan Lau[c], Atindra Krishnan[a], Bruce Dunn[c], Laurent Pilon[a,*]

[a] Mechanical and Aerospace Engineering Department, Henry Samueli School of Engineering and Applied Science, University of California, Los Angeles, CA 90095, USA
[b] Mechanical Engineering Department, King Fahd University of Petroleum and Minerals (KFUPM), Dhahran 31261, Saudi Arabia
[c] Materials Science and Engineering Department, Henry Samueli School of Engineering and Applied Science, University of California, Los Angeles, CA 90095, USA

HIGHLIGHTS

- An isothermal calorimeter was designed, manufactured, and carefully validated.
- The device can measure heat generation rate at each electrode of supercapacitors.
- Its capabilities were illustrated with EDLC electrodes and various electrolytes.
- Irreversible heat generation rate was due to Joule heating.
- Reversible heat generation rate was significantly lower at the negative electrodes.

GRAPHICAL ABSTRACT

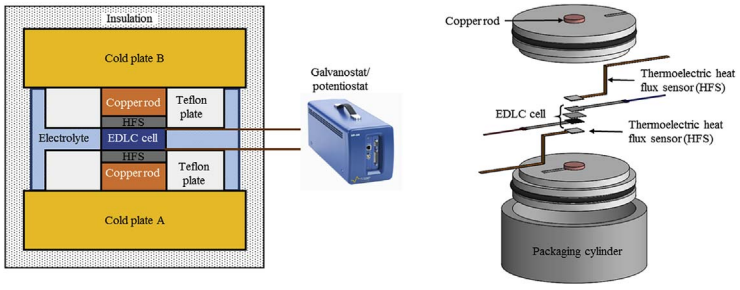

ARTICLE INFO

Keywords:
Isothermal calorimeter
Energy storage
Pseudocapacitors
Supercapacitors
Thermal management
Heat generation

ABSTRACT

Heat generation in electric double layer capacitors (EDLCs) may lead to temperature rise and reduce their lifetime and performance. This study aims to measure the time-dependent heat generation rate in individual carbon electrode of EDLCs under various charging conditions. First, the design, fabrication, and validation of an isothermal calorimeter are presented. The calorimeter consisted of two thermoelectric heat flux sensors connected to a data acquisition system, two identical and cold plates fed with a circulating coolant, and an electrochemical test section connected to a potentiostat/galvanostat system. The EDLC cells consisted of two identical activated carbon electrodes and a separator immersed in an electrolyte. Measurements were performed on three cells with different electrolytes under galvanostatic cycling for different current density and polarity. The measured time-averaged irreversible heat generation rate was in excellent agreement with predictions for Joule heating. The reversible heat generation rate in the positive electrode was exothermic during charging and endothermic during discharging. By contrast, the negative electrode featured both exothermic and endothermic heat generation during both charging and discharging. The results of this study can be used to validate existing thermal models, to develop thermal management strategies, and to gain insight into physicochemical phenomena taking place during operation.

1. Introduction

Electric double layer capacitors (EDLCs) have attracted significant interest as energy storage systems thanks to their large power densities, long cycle life, and high cycle efficiency compared with batteries [1,2]. They are attractive for many applications requiring rapid charging/discharging, such as regenerative braking in hybrid or electric vehicles and renewable energy harvesting systems [2–7]. EDLC devices consist of two carbon-based electrodes and a separator immersed in aqueous or organic electrolytes. They store electric charges in the electric double

* Corresponding author.
E-mail address: pilon@seas.ucla.edu (L. Pilon).

https://doi.org/10.1016/j.jpowsour.2017.11.012
Received 18 August 2017; Received in revised form 2 October 2017; Accepted 4 November 2017

Nomenclature

A	Footprint area of the heat flux sensor, cm^2
c_p	Specific heat, J/(kg·°C)
C_g	Gravimetric capacitance, F/g
I	Current, mA
k	Thermal conductivity, W/(m·°C)
L	Electrode thickness, cm
m	Mass loading of active material in electrode, mg/cm^2
n	Cycle number, -
q	Heat flux, mW/cm^2
$\dot{q}$	Volumetric heat generation rate, mW/cm^3
$\dot{Q}$	Heat generation rate, mW
$\overline{\dot{Q}}$	Time-averaged heat generation rate, mW
R_i	Electric resistance of resistor or electrode "i", Ω
R_s	Internal resistance for entire EDLC device, Ω
S	Heat flux sensor sensitivity, $\mu V/(W/m^2)$
S_o	Heat flux sensor sensitivity at 22.5 °C, $\mu V/(mW/cm^2)$
S_c	Heat flux correction factor, $\mu V/[°C\cdot(mW/cm^2)]$
t	Time, s
t_c^-	Time immediately after the beginning of the discharging step, s
t_c^+	Time at the end of the charging step, s
T_c	Cold plate temperature, °C
T_o	Operating temperature, °C
ΔV	Voltage difference generated in the heat flux sensor, μV

Greek symbols

ν	Scan rate, mV/s
ψ_s	Potential across an EDLC cell, V

Superscripts and subscripts

A or B	Refers to heat flux sensor A or B
c	Refers to charging step
cd	Refers to charging-discharging cycle
d	Refers to discharging step
J	Refers to Joule heating
J, 1 or J, 2	Refers to Joule heating in Resistor 1 or 2
max	Refers to maximum
min	Refers to minimum
T	Refers to entire cell
rev, i	Refers to reversible in electrode "i"
+ or −	Refers to positive or negative electrode

layer (EDL) forming at the mesoporous electrode/electrolyte interfaces.

EDLCs are usually cycled at high current densities resulting in significant amount of volumetric heat generation. This, in turn, can result in excessive temperature rise during normal operation leading to (i) accelerated cell aging [3,4,8–11], (ii) increased self-discharge rates [3,8–10], and possibly (iii) electrolyte decomposition and evaporation [10,12]. Heat generation in EDLCs can be attributed to irreversible and reversible processes. Irreversible heat generation has been shown to correspond to Joule heating [2,8,13–16]. It is proportional to the square of the current and, as such, is always positive. It remains constant throughout the cell under constant current cycling [15–18]. On the other hand, recent physical modeling indicates that reversible heat generation is affected by ion diffusion, steric effects, entropy of mixing, and possible redox reactions [16,18]. It occurs mostly near the electrolyte/electrode interface where the EDL forms [16]. The amount of reversible heat generated in the device during a charging step under constant current cycling has been found, both experimentally [8,15] and theoretically [8,16,17], to be proportional to the current.

The present study aims to measure the instantaneous heat generation rates in each electrode of EDLC devices under galvanostatic cycling in order to improve our understanding of the responsible physiochemical phenomena. To do so, an isothermal calorimeter was designed, assembled, and validated to measure the time-dependent irreversible and reversible heat generation rates in each electrode of electrochemical cells. Several EDLC devices consisting of two identical electrodes made of activated carbon and different aqueous or organic electrolytes were investigated. The results will be instrumental in validating and/or improving existing thermal models and in developing thermal management strategies. They can also be used to give insight in the physicochemical processes involved in charging and discharging of electrochemical energy storage systems.

2. Background

2.1. Thermal models

Several thermal models of EDLCs have been proposed in the literature [3,8–10,15–19]. Most of them aimed to predict the temperature distribution within a cell by solving the energy equation considering Joule heating as the only source of heat generation. By contrast, Schiffer et al. [8] developed a thermal model accounting for reversible heat generation rate through an ad hoc model based on entropy change considerations and experimental observations [8]. Their model assumed that the reversible heat generation rate was proportional to the current [8].

More recently, d'Entremont and Pilon [16] developed a spatio-temporal physical model based on first principles by coupling the heat diffusion equation with the modified Poisson-Nernst-Planck (MPNP) model to derive analytical expressions for both irreversible and reversible heat generation rates in EDLCs. The irreversible heat generation rate was attributed solely to Joule heating. By contrast, the reversible heat generation rate was attributed to diffusion, steric effects, and entropy changes [16]. Numerical simulations of the heat generation rate in a binary and symmetric electrolyte were performed for planar electrodes during constant current cycling. First, the irreversible heat generation rate was found to be proportional to the square of the imposed current I^2. On the other hand, the time-averaged reversible heat generation rate was exothermic during charging and endothermic during discharging and proportional to the imposed current [16]. These results were in qualitative agreement with experimental data reported in the literature [8,19].

D'Entremont and Pilon [17] extended their physical model for heat generation rate in EDLCs to electrolytes consisting of multiple and/or asymmetric ion species with arbitrary ion diameter and diffusion coefficient. They observed that dissimilarity in ion valency, diameter, and/or diffusion coefficient between cations and anions of the electrolyte resulted in different heat generation rates at the two electrodes of EDLC devices [17]. In fact, larger ion valency and/or diffusion coefficient led to smaller irreversible heat generation rate due to an increase in electrolyte electrical conductivity [17]. In addition, the total reversible heat generation rate during charging was larger for smaller ion diameter and/or larger valency [17]. Additionally, d'Entremont and Pilon [18] further extended their model to hybrid pseudocapacitors to account for both electric double layer (EDL) formation and faradaic reactions in the pseudocapacitive electrode. First, carbon electrode exhibited the same thermal behavior observed in EDLC carbon electrodes [16,18]. Second, two regimes of operation were observed at the pseudocapacitive electrode namely a faradaic and a capacitive regime [18]. The faradaic regime occurred at low current densities and slow charging/discharging when the heat generation rate associated with

faradaic reactions at the pseudocapacitive electrode dominated over the other sources of reversible heat generation rate [18]. On the other hand, the capacitive regime occurred at high current densities and fast charging/discharging when the heat generation rate, due to EDL formation, dominated over the reversible heat generation rate due to faradaic reactions. Finally, by contrast with carbon electrode, the reversible heat generation rate associated with EDL formation at the pseudocapacitive electrode was both exothermic and endothermic during either charging or discharging [18]. The authors attributed this to the asymmetric evolution of ion concentrations at the pseudocapacitive electrode due to faradaic reactions [18].

2.2. Experimental measurements

Both accelerated rate and isothermal calorimeters have been used to investigate heat generation in electrical energy storage devices including batteries [14,20–26] and electrochemical capacitors [15,27]. In accelerated rate calorimeter, part of the heat generated in the test cell is transferred to a constant temperature source while the rest remained confined into the cell [28]. This can lead to excessive rise in the cell temperature leading to damage to cell components. By contrast, in isothermal calorimeter, the test section is maintained at constant temperature during operation thanks to a large isothermal heat sink in thermal contact with the test section. Isothermal calorimeter usually requires special data processing. For example, Dandeville et al. [15] used deconvolution analysis to estimate the heat generation rate from measured temporal temperature evolution of the cell. This approach also requires that the calorimeter thermal impedance be determined experimentally. In addition, time correction to the deconvoluted heat generation rate can be considered to account for the instrument time lag [14,21,22,24].

Moreover, reversible heat generation in EDLCs was ignored in many previous experimental studies [3,9,10,27]. To the best of our knowledge, it was first observed experimentally by Schiffer et al. [8] in commercial EDLCs (including packaging) under constant current cycling. The measurements were performed in a quasi-adiabatic polystyrene box [8]. Thermocouples were placed at different locations on the external surface of the device. The measured temperatures featured temporal oscillations around a linear rise. The average temperature rise was attributed to Joule heating while the temperature oscillations were attributed to reversible heat generation due to entropy changes [8]. During charging, the ions formed an EDL at the electrode/electrolyte interface and thus lowered their entropy and released heat [8]. On the other hand, during discharging, the ions' entropy increased and heat was absorbed as they dispersed into the electrolyte [8].

Gualous et al. [9] investigated heat generation in commercial EDLCs by placing thermocouples on their outer surfaces subjected to cooling by natural convection. The temporal temperature oscillations were not observed because of poor placement of the thermocouples. However, Gualous et al. [19] modified their previous apparatus [9] by placing thermocouples inside and along the radial axis of a commercial EDLC. Then, temperature oscillations with time were observed. The average temperature and the oscillation amplitude decreased along the radial direction of the cylindrical device due to convective cooling at the outer surface [9]. Unfortunately, the measurements performed in Refs. [8,9,19] only provided the temperature evolution while the heat generation was predicted using an ad hoc model. In addition, the relatively large size of the EDLC devices tested and the placement of the thermocouples could result in delay in temperature measurements due to the device's thermal mass [8,9,19].

Pascot et al. [27] and Dandeville et al. [15] designed and assembled a non-adiabatic calorimetric apparatus to obtain heat generation rate in EDLCs and hybrid pseudocapacitors by measuring the temperature evolution of the devices. The apparatus consisted of (i) a test cell with carbon-based and MnO_2 pseudocapacitive electrodes inserted in (ii) a bath of aqueous electrolyte, (iii) a custom-made heat flux meter, and (iv) two cold plates maintained at constant and identical temperature. The electrolyte bath was injected with nitrogen bubbles to minimize temperature fluctuations and prevent electrode oxidation. Each heat flux meter was made of 16 thermocouples connected in series and embedded in a polyphenylene sulfide plate. The heat generation rate was obtained by deconvolving the temperature difference measured between the test cell and the cold plates as a function of time. The apparatus was able to achieve a sensitivity of 630 μV/°C for the measured voltage and 0.001°C for the detected temperature difference [15]. EDLC (carbon-carbon) and hybrid pseudocapacitor (carbon-MnO_2) two-electrode devices were tested in 0.5 M aqueous K_2SO_4 electrolyte under galvanostatic cycling. The authors assumed that (i) the heat generation rate was identical in both carbon electrodes of the EDLC and that (ii) the heat generation rate in a carbon electrode of the EDLC was identical to that in the carbon electrode of the hybrid pseudocapacitor, for a given constant current. Then, the instantaneous heat generation rate in the MnO_2 electrode was obtained by subtracting the heat generation rate measured in the carbon electrodes of the EDLC from the total heat generation rate measured in the hybrid pseudocapacitor. The carbon electrodes in the EDLC device heated during charging and cooled

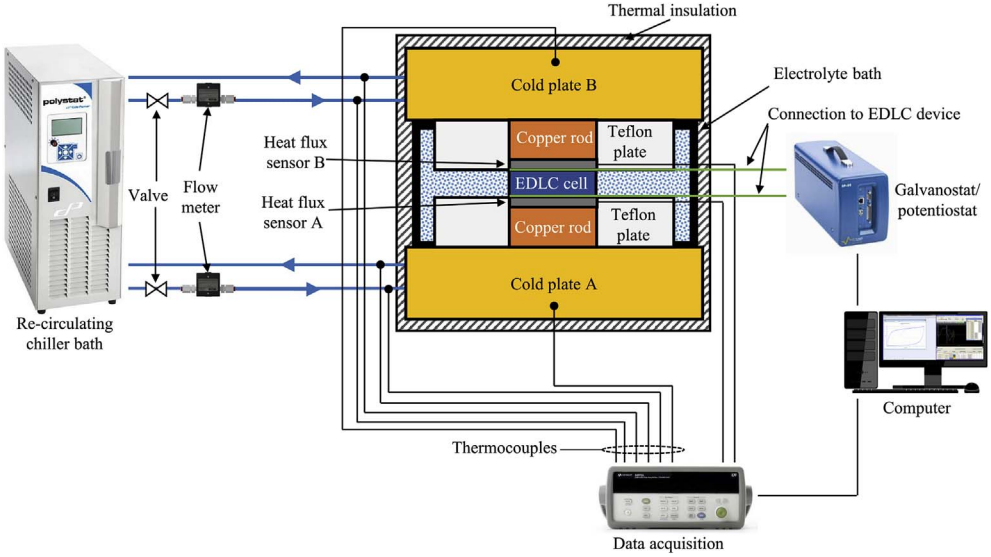

Fig. 1. Schematic of an isothermal calorimeter apparatus designed and fabricated in the present study to measure heat generation rate in EDLCs.

during discharging which was attributed to ions adsorption and desorption at the porous carbon electrode surface [15]. By contrast, the MnO_2 electrode exhibited cooling during charging and heating during discharging [15]. The authors attributed the reversible heating in the MnO_2 electrode to reversible redox reactions along with ions adsorption and desorption [15]. Finally, the irreversible heat generation rate averaged over a cycle and the reversible heat generation rate averaged over a charging step were proportional to I^2 and I, respectively [15].

The present study aims to develop an isothermal calorimeter that can measure accurately the instantaneous heat generation rate in each individual electrode of EDLC or hybrid pseudocapacitor devices. This calorimeter was used to gain insight in the physicochemical phenomena responsible for irreversible and reversible heat generation in EDLCs consisting of activated carbon electrodes with different aqueous and organic electrolytes. In particular, it aims to determine whether heat generation is the same in the two identical electrodes of an EDLC device and to assess the effect of electrolyte and cell polarity.

3. Materials and methods

3.1. Isothermal calorimeter

An isothermal calorimeter was designed, fabricated, and validated to measure instantaneous heat generation rate in electrical energy storage systems. Fig. 1 schematically shows the entire experimental apparatus including (i) two thermoelectric heat flux sensors (HFS) connected to (ii) a data acquisition (DAQ) system (34972A LXI, Keysight Technology), (iii) two identical instrumented cold plates fed with a circulating heat transfer fluid (Dynalene HC-50, Dynalene Inc.) from (iv) a temperature-controlled chiller (Polystat, Cole-Parmer), (v) two flow meters (FLR-1012, Omega), and (vi) an electrochemical test section containing a two-electrode cell immersed in an electrolyte and connected to (vii) a potentiostat/galvanostat (SP 150, Bio-Logic Science Instruments). The voltage measured by the DAQ reading the heat flux sensors featured accuracy of $\pm 0.1\ \mu V$. The potentiostat/galvanostat system was operated at constant current, i.e., in galvanostatic charging-discharging mode, with current ranging from ± 0.01 to ± 800 mA with resolution of 0.76 nA. The materials of the electrochemical test section and the cooling fluid were selected to cover a broad range of operating temperature ranging from − 40°C to 70°C. A vertical clamp was used to hold the electrochemical test section and the cold plates together and to ensure good thermal contacts among them. Finally, the entire calorimeter and the cold plates were wrapped in 13 mm thick thermal insulation (Ceramic fiber, Morgan Thermal Ceramics), with thermal conductivity of 0.07 W/m.K to minimize heat losses to the surrounding.

Fig. 2 shows (a) an exploded view of the apparatus, (b) an enlarged view of the sensing area, (c) photograph of a typical $1 \times 1\ cm^2$ activated carbon electrode supported by a 316 stainless steel current collector, and (d) a cross-sectional view of a heat flux sensor plate with the corresponding dimensions. The electrochemical test section consisted of two heat flux sensor plates and a cylindrical container made of polytetrafluoroethylene (PTFE) or Teflon. The latter offers many benefits

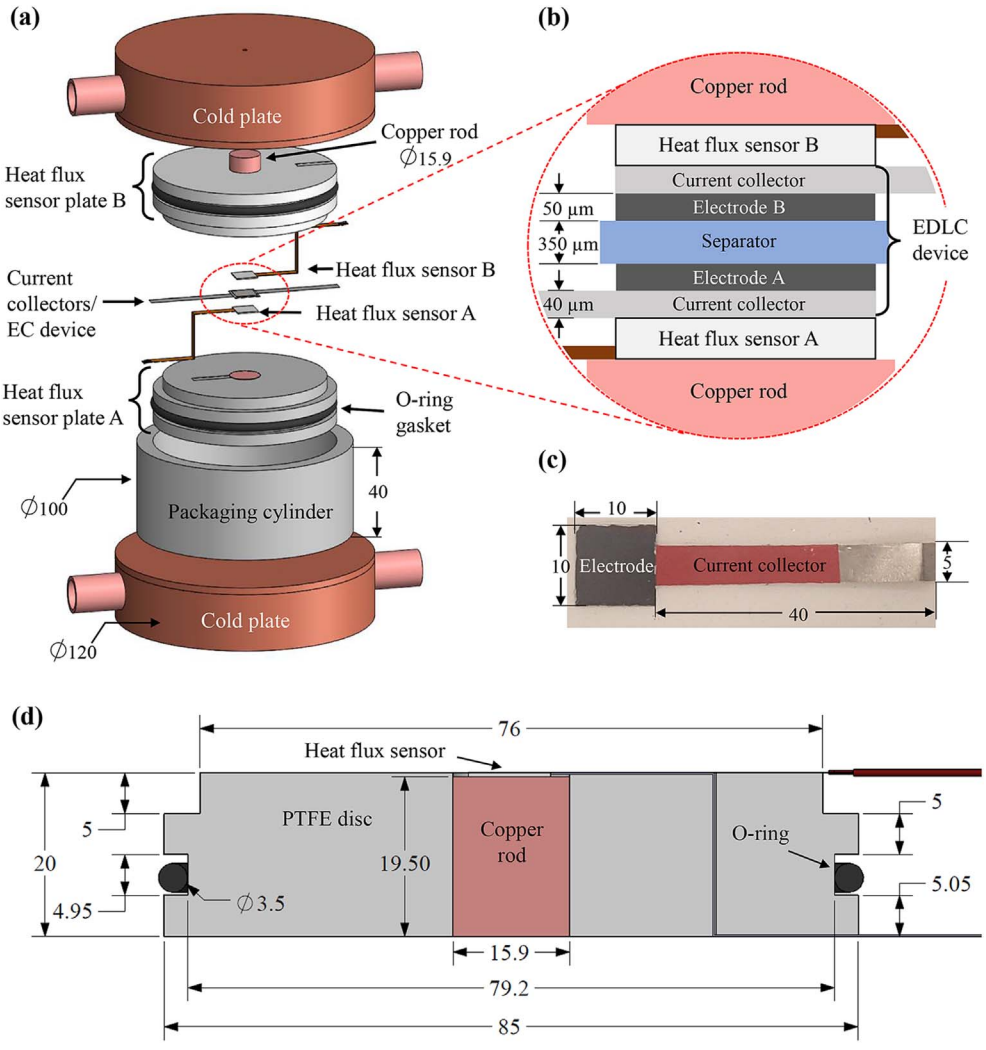

Fig. 2. (a) Exploded and (b) enlarge view of the test area, (c) photograph of a 1×1 cm^2 activated carbon electrode supported by a 316 stainless steel current collector, and (d) cross-section view of a heat flux sensor plate with corresponding dimensions (all dimensions in mm).

including (i) thermal and mechanical stabilities over a wide range of temperature (i.e. −200°C to 260°C), (ii) low thermal conductivity of 0.25 W/m.K, and (iii) chemical resistance to strong acids and bases, making it safe to be in contact with any electrolyte. Each heat flux sensor plate consisted of (i) 10 × 10 mm thermoelectric heat flux sensor (gSKIN-XP, greenTEG), 0.5 mm in thickness, in thermal contact with (ii) a cylindrical copper rod, 15.9 mm in diameter and 19.5 mm in length, embedded in the center of (iii) a PTFE disc and flush with its surfaces. The thickness and diameter of the PTFE disc were 20 mm and 85 mm, respectively. The copper rod was used to conduct the heat generated in the electrode through the heat flux sensor to the cold plate, maintained at constant temperature. The two heat flux sensor plates were packaged in a 7.5 mm thick PTFE cylinder with height and outer diameter of 40 mm and 100 mm, respectively. Each plate was sealed using a chemical-resistance O-ring gasket (Viton-235, MSCdirect) 3.5 mm in thickness and 86 mm in outer diameter to prevent electrolyte evaporation and interaction with surrounding air. The electrochemical test section containing the EDLC device was assembled in a glove box under inert conditions before being transferred to the isothermal calorimeter.

3.2. Data analysis

The thermoelectric heat flux sensors operated based on the Seebeck effect to directly measure heat flux as low as 10 μW/cm^2 with uncertainty of ± 3% [29]. The temperature differences between the positive and negative electrodes and the cold plates imposed across the heat flux sensors A or B resulted in a voltage difference ΔV_j proportional to the heat flux $q_j^{''}$ at the heat flux sensor/electrode interface given by Ref. [29],

$$q_j'' = \frac{\Delta V_j}{S_j} \quad \text{with } j = \text{A or B.} \tag{1}$$

Here, S_j is the sensor temperature-dependent sensitivity expressed as [29],

$$S_j = S_{o,j} + (T_o - 22.5)S_{c,j} \quad \text{with } j\text{=A or B} \tag{2}$$

where $S_{o,j}$ and $S_{c,j}$ are the sensor sensitivity at 22.5°C and a temperature correction factor, respectively. Each heat flux sensor was calibrated independently by the manufacturer according to ISO standard 8301 [30]. The parameters $S_{o,j}$ and $S_{c,j}$ for heat flux sensor A were provided as $S_{o,A}$= 131.9 μV/(mW/cm^2) and $S_{c,A}$= 0.161 μV/[°C·mW/cm^2)] while those for heat flux sensor B were $S_{o,B}$= 118.3 μV/(mW/cm^2) and $S_{o,B}$= 0.143 μV/[°C·mW/cm^2)].

Based on simple heat transfer arguments assuming that the electrodes of the EDLC device are thermally insulated from one another and ignoring thermal inertia, one can show that the instantaneous heat generation rate $\dot{Q}(t)$ (in mW) in electrode "*i*" in contact with heat flux sensor "*j*" can be expressed as (see Supplementary Materials),

$$\dot{Q}_i(t) = q_j^{''} A_i = q_i^{''} A_i = \frac{\Delta V_i(t)}{S_i} A_i \quad \text{with } i = +\text{or}- \tag{3}$$

where A_i is the footprint area of the electrode. Here, the subscript "*i*" refers to the positive "+" or negative "−" electrode.

The time-averaged heat generation rate $\bar{\dot{Q}}_i$ at electrode "*i*" subjected to a galvanostatic cycle of period t_{cd} was estimated by integrating the instantaneous heat generation rate $\dot{Q}_i(t)$ over one period, i.e.,

$$\bar{\dot{Q}}_i = \frac{1}{t_{cd}} \int_{(n-1)t_{cd}}^{nt_{cd}} \dot{Q}_i(t)dt \quad \text{with } i = +\text{or}- \tag{4}$$

where *n* is the cycle number, large enough to have reached oscillatory steady state. In addition, the instantaneous reversible heat generation rate $\dot{Q}_{rev,i}(t)$ at each electrode can be evaluated by subtracting the time-averaged heat generation rate $\bar{\dot{Q}}_i$ [Equation (4)] from the instantaneous heat generation rate $\dot{Q}_i(t)$, i.e.,

$$\dot{Q}_{rev,i}(t) = \dot{Q}_i(t) - \bar{\dot{Q}}_i \quad \text{with } i = +\text{or} - . \tag{5}$$

In order to effectively compare the reversible heat generation rate at each electrode, the instantaneous reversible heat generation rate $\dot{Q}_{rev,i}(t)$ was averaged over a galvanostatic charging step of duration t_c to yield,

$$\bar{\dot{Q}}^c_{rev,i} = \frac{1}{t_c} \int_{(n-1)t_{cd}}^{(n-1)t_{cd}+t_c} \dot{Q}_{rev,i}(t)\, dt \qquad \text{with } i = +, \text{ or } - . \tag{6}$$

Note that, by definition, time-averaging of the reversible heat generation rate $\dot{Q}_{rev,i}(t)$ at electrode "*i*" over an entire galvanostatic cycle of period t_{cd} yields $\bar{\dot{Q}}_{rev,i} = 0$.

Finally, the total instantaneous, time-averaged, reversible, and time-averaged of reversible heat generation rates in the entire cell can be expressed as $\dot{Q}_T(t) = \dot{Q}_+(t) + \dot{Q}_-(t)$, $\bar{\dot{Q}}_T = \bar{\dot{Q}}_+ + \bar{\dot{Q}}_-$, $\dot{Q}_{rev,T}(t) = \dot{Q}_{rev,+}(t) + \dot{Q}_{rev,-}(t)$, and $\bar{\dot{Q}}^c_{rev,T} = \bar{\dot{Q}}^c_{rev,+} + \bar{\dot{Q}}^c_{rev,-}$, respectively.

3.3. Validation

In order to validate the isothermal calorimeter apparatus and the associated data analysis described previously, two resistors were connected in series and separated by a 0.35 mm thick porous glass fiber separator (GF 85 filter, Inc.) identical to that later used in the EDLC devices. Resistors 1 and 2 were made of 10 mm × 2 mm 316 stainless steel plates respectively 50 μm and 90 μm in thickness resulting in electric resistance measured as R_1 = 68 mΩ and R_2 = 40 mΩ. The resistors were connected in series by a 0.2 mm diameter copper wire. The stack of Resistor 1/separator/Resistor 2 was placed in the electrochemical test section between the thermoelectric heat flux sensors either in air (dry) or in deionized (DI) water (wet) to emulate heat generation in EDLCs during charging and discharging. Cycling was performed on resistors R_1 and R_2 by imposing a constant current *I*, between 50 and 150 mA, for 10 s followed by zero current for 10 s. The cold plates were maintained at constant temperature T_c = 20°C.

Fig. 3(a) shows five galvanostatic cycles of the imposed current $I(t)$ as a function of time and the resulting heat generation rate $\dot{Q}_i(t)$ in each resistor for I = 150 mA under dry conditions. It is interesting to note that the measured heat generation rate $\dot{Q}_i(t)$ featured fast response to any change in the imposed current *I*. The time response was less than 1 s confirming that thermal inertia was negligible given the small size of the resistors. Fig. 3(a) also indicates that the measurement noise for $\dot{Q}_i(t)$ was negligibly small. Fig. 3(b) shows the time-averaged heat generation rates $\bar{\dot{Q}}_1$ and $\bar{\dot{Q}}_2$ in resistors R_1 and R_2 as functions of I^2 for current *I* ranging between 50 and 150 mA for both dry and wet conditions. Here, time-averaging of $\bar{\dot{Q}}_i$ was performed for 30 consecutive cycles. The error bars correspond to two standard deviations or 95% confidence interval. It is interesting to note that the measured heat generation rates $\bar{\dot{Q}}_i$ were identical whether the resistors and separator were in air or immersed in DI water with thermal conductivity of 0.62 W/m.K [31]. In other words, heat conduction from a given resistor through the separator in air or water was negligible compared with the heat conducted through the heat flux sensors. This observation confirms the assumptions used to derive Equation (3). Fig. 3(b) also plots the heat generation rate estimated for Joule heating within each resistor given by $\bar{\dot{Q}}_{J,i} = R_i I^2$. Excellent agreement was found between measured and predicted values of $\bar{\dot{Q}}_i$ for all current *I* considered. These validation results confirm that the apparatus can measure separately the time-dependent heat generation rates within each electrode of an electrical energy storage device.

3.4. EDLC device

Three EDLC devices were tested (i) to demonstrate the capability of the apparatus in measuring the instantaneous heat generation rate at

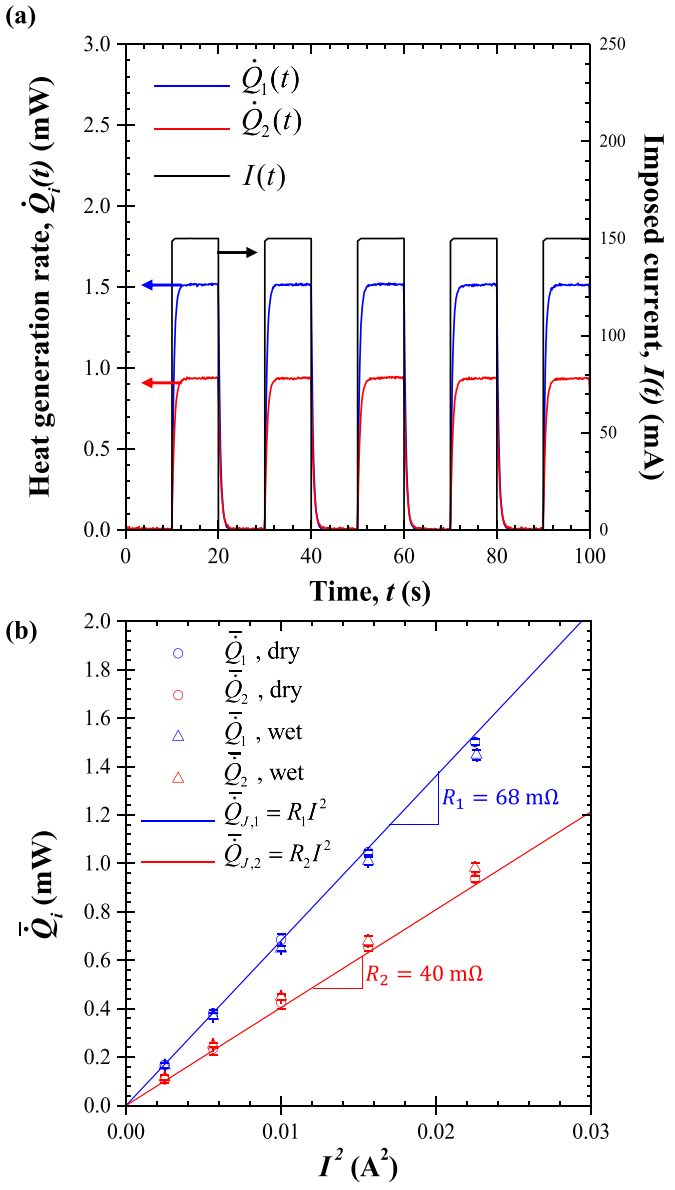

Fig. 3. (a) Temporal evolution of the imposed current $I(t)$ and the resulting heat generation rate $\dot{Q}_i(t)$ in resistors R_1 and R_2 for I = 150 mA for dry conditions. (b) Time-averaged heat generation rates $\bar{\dot{Q}}_i$ measured in resistors R_1 and R_2 as functions of I^2 and predictions for Joule heat generation rate given by $\bar{\dot{Q}}_{J,i} = R_i I^2$.

each electrode of EDLC cells, (ii) to gain insight into the physical phenomena responsible for heat generation therein, and (iii) to assess previous experimental measurements [8,15,19] and validate our recent physicochemical models [16,17].

EDLC electrodes were made of activated carbon (YP50F, Kuraray Chemical) with a surface area of 300 m^2/g and pore size less than 2 nm [32]. The electrodes were synthesized by mixing, in DI water, 80 wt% of YP50F, 5 wt% of TX100 surfactant, 1.5 wt% of carboxymethyl cellulose (CMC) used as a thickening agent/binder, and 13.5 wt% of styrene butadiene rubber (SBR) used as a binder. The resulting slurry was drop casted onto a 1 × 1 cm^2 316 stainless steel plates, serving as current collectors. The latter had been previously treated by oxygen plasma to enhance their hydrophilicity and ensure even spreading of the slurry. The mass loading, for each electrode, was 2 mg of activated carbon per cm^2 with a thickness of 50 ± 5 μm. The electrodes were dried under vacuum at 120°C for 24 h before being placed in a glove box under argon atmosphere.

The EDLC devices tested consisted of two identical activated carbon

Table 1
Electrolyte composition and galvanostatic operating conditions for the three carbon-based EDLC cells studied.

Device No.	Salt	Solvent	Potential window ($\psi_{min} - \psi_{max}$) (V)
1	1 M $LiPF_6$	EC:DMC (1:1)	0–1
2	1 M citric acid	DI water	0–0.8
3	1 M TBATFB	Acetonitrile	0–1

electrodes separated by a 350 μm glass fiber separator (GF85 filter, Advantec MFS Inc.) identical to that used for validation of the apparatus with the resistors. Different electrolytes and associated potential windows were tested to assess the effect of ions size and valency and their asymmetry on the performance and thermal behavior of EDLC devices, as summarized in Table 1. Devices 1 and 3 used organic electrolytes made of (i) 1 M of lithium hexafluorophosphate ($LiPF_6$) in ethylene carbonate:dimethyl carbonate (EC:DMC) with 1:1 volume ratio and (ii) 1 M of tetrabutylammonium tetrafluoroborate (TBATFB) in acetonitrile solvent, respectively. By contrast, Device 2 used an aqueous electrolyte made of 1 M of citric acid in deionized (DI) water. Citric acid was chosen because it does not corrode the stainless steel current collector, unlike most aqueous electrolytes. Thermal conductivities of ethylene carbonate, dimethyl carbonate, and acetonitrile were 0.2 [33], 0.16 [34], and 0.2 W/m.K [35], respectively. These low thermal conductivities ensured that the experimental validation performed using two resistors and separator immersed in DI water was also valid here.

Finally, as previously discussed, each EDLC device was assembled, installed, and sealed in the electrochemical test section inside the glove box to avoid any contact with air. The potential window for Devices 1 and 3 was between ψ_{min} = 0 V and ψ_{max} = 1 V while that for Device 2 was between 0 and 0.8 V since cyclic voltammetry curves of Device 2 featured sharp increase in the current above 0.8 V. The same potential window was used for both aqueous and organic electrolytes to facilitate comparison.

4. Results and discussion

4.1. Gravimetric capacitance C_g

Cyclic voltammetry (CV) was used to determine the gravimetric capacitance of the three EDLC devices previously described. Fig. 4 plots the CV curves of current I (in mA) versus imposed potential $\psi_s(t)$ measured for (a) Device 1, (b) Device 2, and (c) Device 3 for different scan rates ν ranging from 1 to 20 mV/s. The CV curves for Devices 1 and 3 featured rectangular shapes characteristic of EDLCs. However, for Device 2, CV curves deviated from this typical behavior at high scan rates due to apparent resistive losses. Moreover, the cell's gravimetric integral capacitance C_g (in F/g) can be evaluated by integrating the area enclosed by the CV curve for a given scan rate ν as [36],

$$C_g(\nu) = \frac{1}{m(\psi_{max} - \psi_{min})} \oint \frac{I}{2\nu} d\psi \tag{7}$$

where m is the mass of active materials loaded in the electrode. Fig. 4(d) plots the gravimetric capacitance $C_g(\nu)$ of the three EDLC devices as a function of scan rate ν. For all three devices, the gravimetric capacitance decreased with increasing scan rate with the capacitance of Device 2 decreasing faster than that of the other devices.

4.2. Internal resistance R_s

Internal resistance R_s (or DC resistance) of an EDLC is an essential parameter to evaluate the power dissipation in the device. IR drop at the charging/discharging transition during galvanostatic cycling under

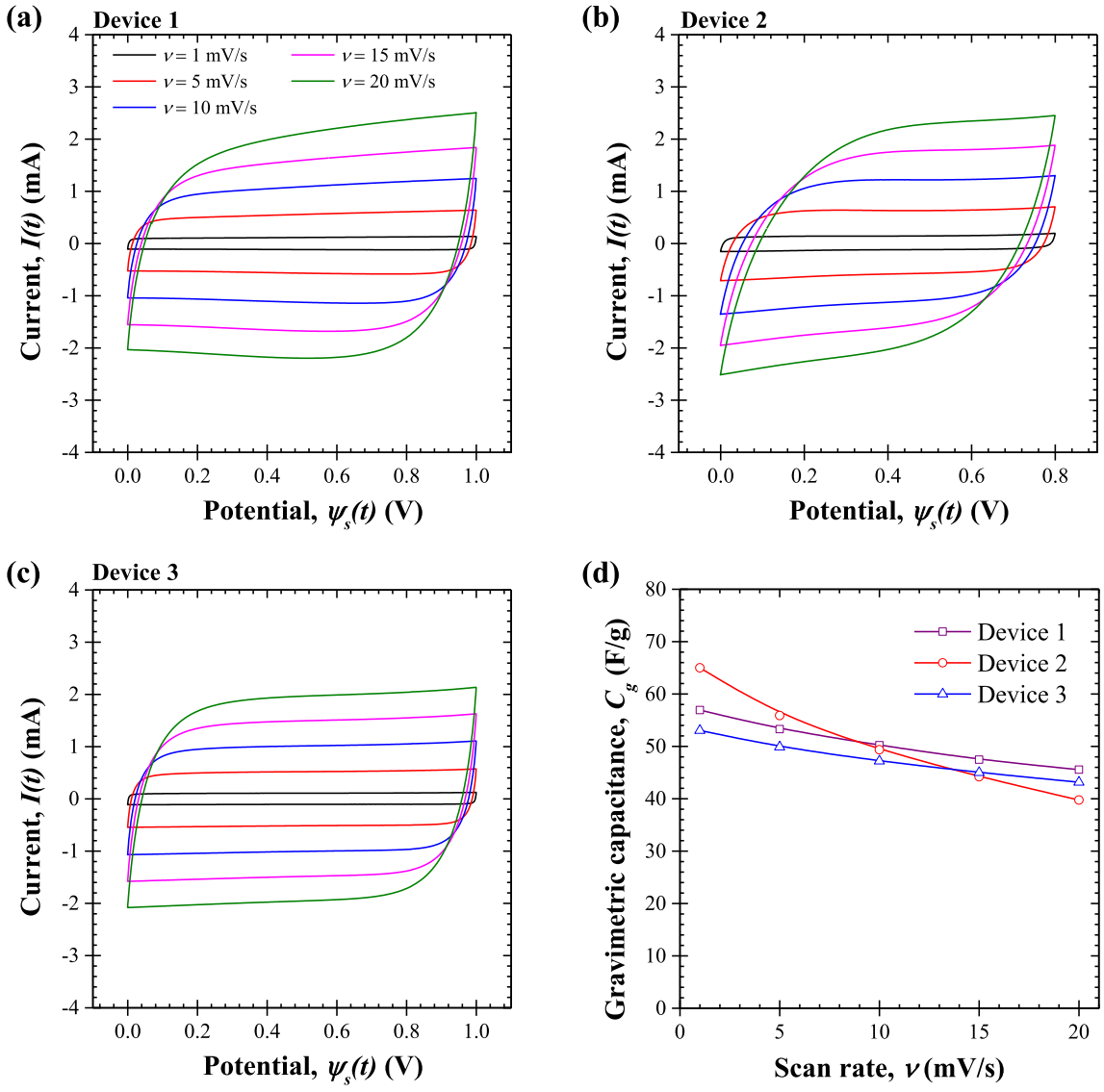

Fig. 4. CV curves for (a) Device 1, (b) Device 2, and (c) Device 3 (see Table 1) for scan rates ν ranging from 1 to 20 mV/s and potential window of 1 V (Devices 1 and 3) and 0.8 V (Device 2) (d) Gravimetric capacitance C_g of Devices 1 to 3 as a function of scan rate ν.

constant current I has been widely used to determine the internal resistance R_s according to [37–39],

$$R_s(I) = \frac{\psi_s(t_c^+) - \psi_s(t_c^-)}{2I} \tag{8}$$

where $\psi_s(t_c^+)$ and $\psi_s\psi_s(t_c^-)$ are respectively the potentials across the EDLC cell at the end of the charging step and immediately after the beginning of the discharging step, as illustrated in Fig. 5(b). Indeed, Fig. 5 shows the potential $\psi_s(t)$ across the cell as a function of time t during galvanostatic cycling for (a) Device 1, (b) Device 2, and (c) Device 3 for current I ranging from 2 to 6 mA. For all three devices, the potential varied almost linearly with time between a minimum potential ψ_{min} and a maximum potential ψ_{max} (Table 1). Nevertheless, the charging-discharging curves featured an IR drop caused by the internal resistance R_s of the EDLC estimated from Equation (8). Fig. 5(d) plots the internal resistance $R_s(I)$ as a function of current I for Devices 1 to 3. In all cases, the internal resistance was nearly independent of current I. In addition, Devices 1 and 3 had similar resistance R_s while Device 2 featured twice as large resistance. This difference was due to the fact that citric acid is a weak electrolyte that only partially dissociates in solution [40,41]. This resulted in larger electrical resistance (Fig. 5(d)) and faster drop in the gravimetric capacitance (Fig. 4(d)) in Device 2 compared with Devices 1 and 3.

4.3. Instantaneous and time-averaged heat generation rates

Fig. 6 shows the temporal evolution of the heat generation rates $\dot{Q}_+(t)$ at the positive electrode, $\dot{Q}_-(t)$ at the negative electrode, and $\dot{Q}_T(t) = \dot{Q}_+(t) + \dot{Q}_-(t)$ in the entire cell as functions of dimensionless time t/t_{cd} for five consecutive galvanostatic cycles under constant current $I = 6$ mA for (a) Device 1, (b) Device 2, and (c) Device 3. It is evident that measurements of the instantaneous heat generation rates $\dot{Q}_+(t)$ and $\dot{Q}_-(t)$ were repeatable cycle after cycle. However, their respective magnitude and shape differed significantly for a given device and among the three devices considered.

Fig. 6 also shows the corresponding time-averaged heat generation rates $\overline{\dot{Q}_+}$, $\overline{\dot{Q}_-}$, and $\overline{\dot{Q}_T}$ under galvanostatic cycling as functions of I^2 for constant current I ranging between 2 and 6 mA for (d) Device 1, (e) Device 2, and (f) Device 3. The error bars correspond to two standard deviations or 95% confidence interval estimated by evaluating $\overline{\dot{Q}_i}$ for 10 consecutive galvanostatic cycles. Physically, $\overline{\dot{Q}_+}$, $\overline{\dot{Q}_-}$, and $\overline{\dot{Q}_T}$ corresponded to irreversible heat generation in individual electrode and

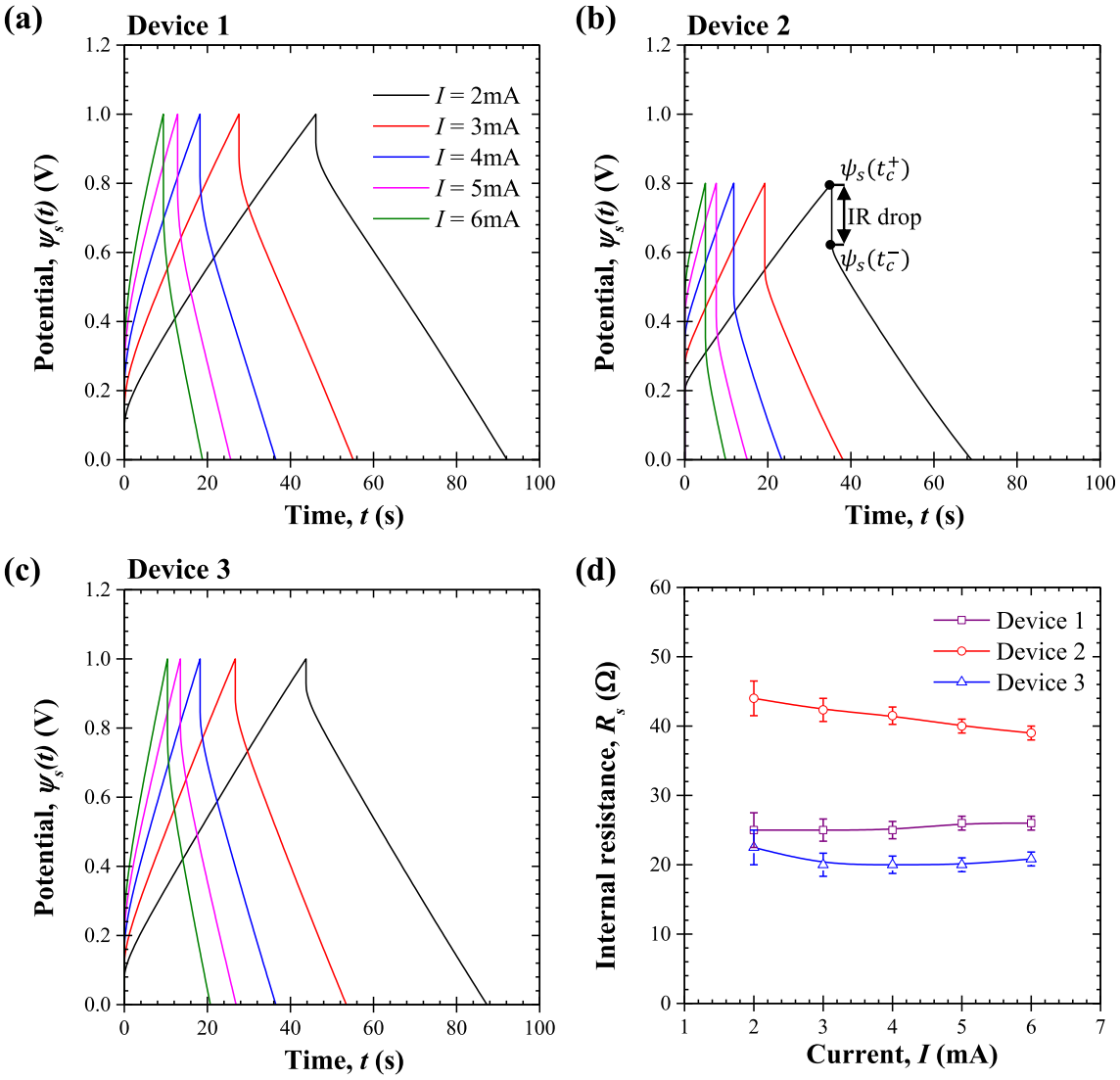

Fig. 5. Potential across the EDLC cell during galvanostatic cycling for (a) Device 1, (b) Device 2, and (c) Device 3 (Table 1) for current I ranging from 2 to 6 mA (d) Internal resistance R_s, determined from IR drop, as a function of current I for all three devices.

in the entire device, respectively. Fig. 6 indicates that the irreversible heat generation rates $\bar{Q}_+$ and $\bar{Q}_-$ were positive and proportional to the square of the current I^2 in both positive and negative electrodes with a coefficient of proportionality corresponding to their respective resistances R_+ and R_-, i.e., $\bar{Q}_+ = R_+I^2$ and $\bar{Q}_- = R_-I^2$. For all EDLC devices considered, minor differences (within 2.3 Ω) were observed between resistances R_+ and R_-. These results confirm that the two electrodes constituting the device were nearly identical.

Finally, Figs. 6(d) and 6(f) indicate that the measured total irreversible heat generation rate $\bar{Q}_T$ was in excellent agreement with predictions for the heat generation rate $\bar{Q}_J$ due to Joule heating in the entire device given by,

$$\bar{Q}_J = R_s(I)I^2 \tag{9}$$

where $R_s(I)$ is the device resistance measured by IR drop (Fig. 5(d)). Note also that the sum of R_+ and R_- matched the total device resistance R_s measured from IR drop (Fig. 5(d)), i.e., $R_s \simeq R_+ + R_-$. Overall, Joule heating was the dominant source of irreversible heat generation at each electrode in the three EDLC devices considered (Table 1). Thus, since Device 2 featured larger internal resistance than Devices 1 and 3, the total time-averaged heat generation rate $\bar{Q}_T$ for Device 2 was also larger than that of Devices 1 and 3.

4.4. Reversible heat generation rates

Fig. 7 shows the instantaneous reversible heat generation rates (a) $\dot{Q}_{rev,T}(t)$ in the entire cell, (b) $\dot{Q}_{rev,+}(t)$ at the positive electrode, and (c) $\dot{Q}_{rev,-}(t)$ at the negative electrode as functions of dimensionless time t/t_{cd} for current I = 6 mA for Devices 1, 2, and 3. Two different cycles were plotted for each device, namely cycle 10 (solid line) and cycle 15 (dashed line). First, Figs. 7(a) and 7(c) establish that $\dot{Q}_{rev,T}(t)$, $\dot{Q}_{rev,+}(t)$, and $\dot{Q}_{rev,-}(t)$ were reproducible from cycle to cycle and followed similar behavior for all devices considered. Fig. 7(a) indicates that the total reversible heat generation rate $\dot{Q}_{rev,T}(t)$ for the entire cell was exothermic for most of the charging step and endothermic during most of the discharging step. These findings were consistent with previous measurements of reversible heat generation in EDLC devices [8,15,16]. However, it is interesting to note that the reversible heat generation rate $\dot{Q}_{rev,+}(t)$ at the positive electrode (Fig. 7(b)) was systematically larger than $\dot{Q}_{rev,-}(t)$ at the negative electrode (Fig. 7(c)), despite the fact that the two electrodes were identical. In fact, the heat generation rate $\dot{Q}_{rev,+}(t)$ was also exothermic during charging and endothermic during discharging suggesting that the thermal behavior of the positive electrode was in agreement with our expectation and with the literature [8,15–17]. On the other hand, the heat generation rate $\dot{Q}_{rev,-}(t)$ at the negative electrode was both exothermic and endothermic during either

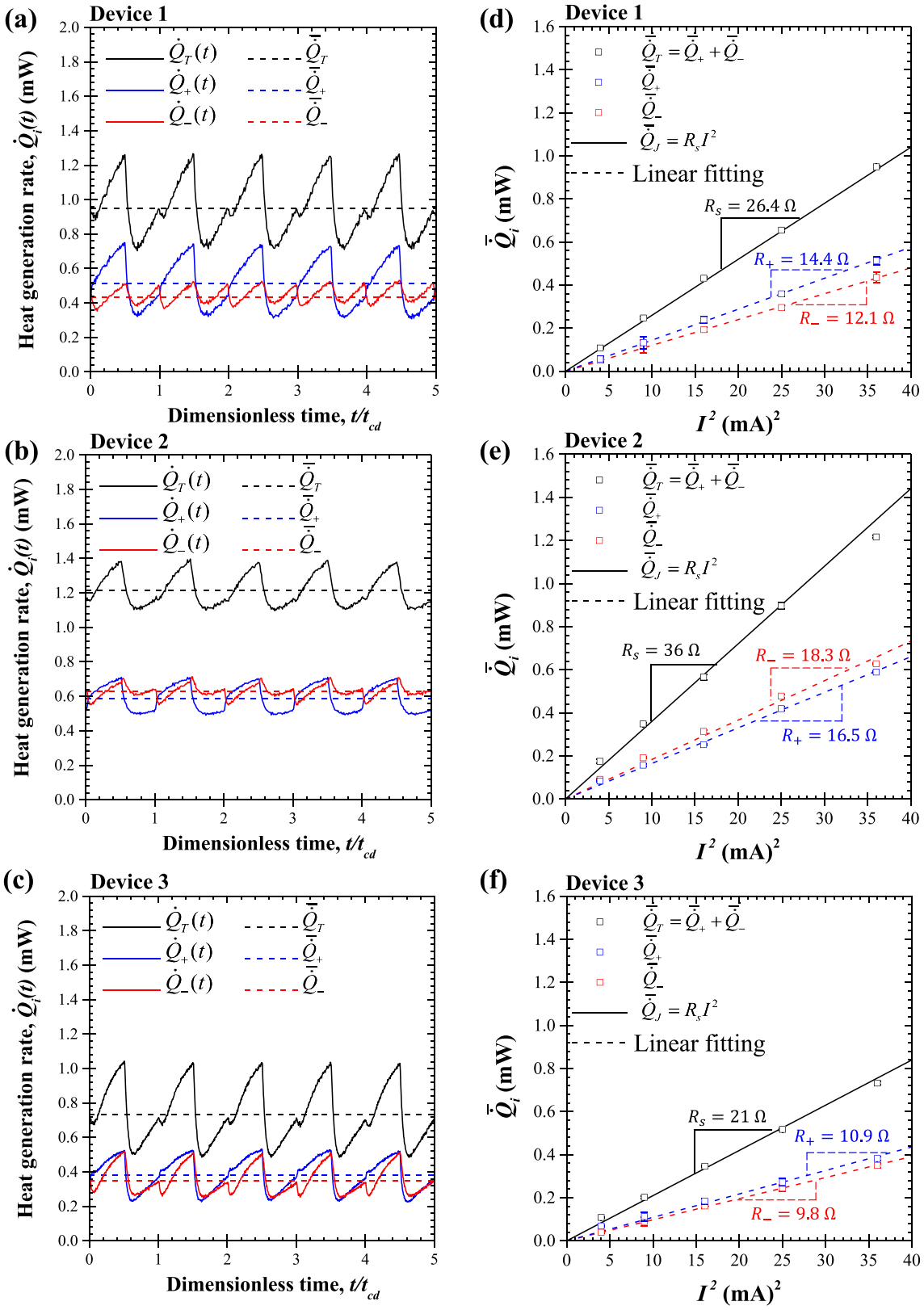

Fig. 6. Heat generation rates $\dot{Q}_+(t)$ at the positive electrode (blue), $\dot{Q}_-(t)$ at the negative electrode (red), and $\dot{Q}_T(t)$ in the entire cell (black) as functions of the dimensionless time t/t_{cd} for current I = 6 mA for (a) Device 1, (b) Device 2, and (c) Device 3 for five galvanostatic cycles. Time-averaged heat generation rates $\bar{Q}_+$, $\bar{Q}_-$, and $\bar{Q}_T$ under galvanostatic cycling as functions of I^2 for current I ranging between 2 and 6 mA for (d) Device 1, (e) Device 2, and (f) Device 3 (Table 1). (For interpretation of the references to colour in this figure legend, the reader is referred to the web version of this article.)

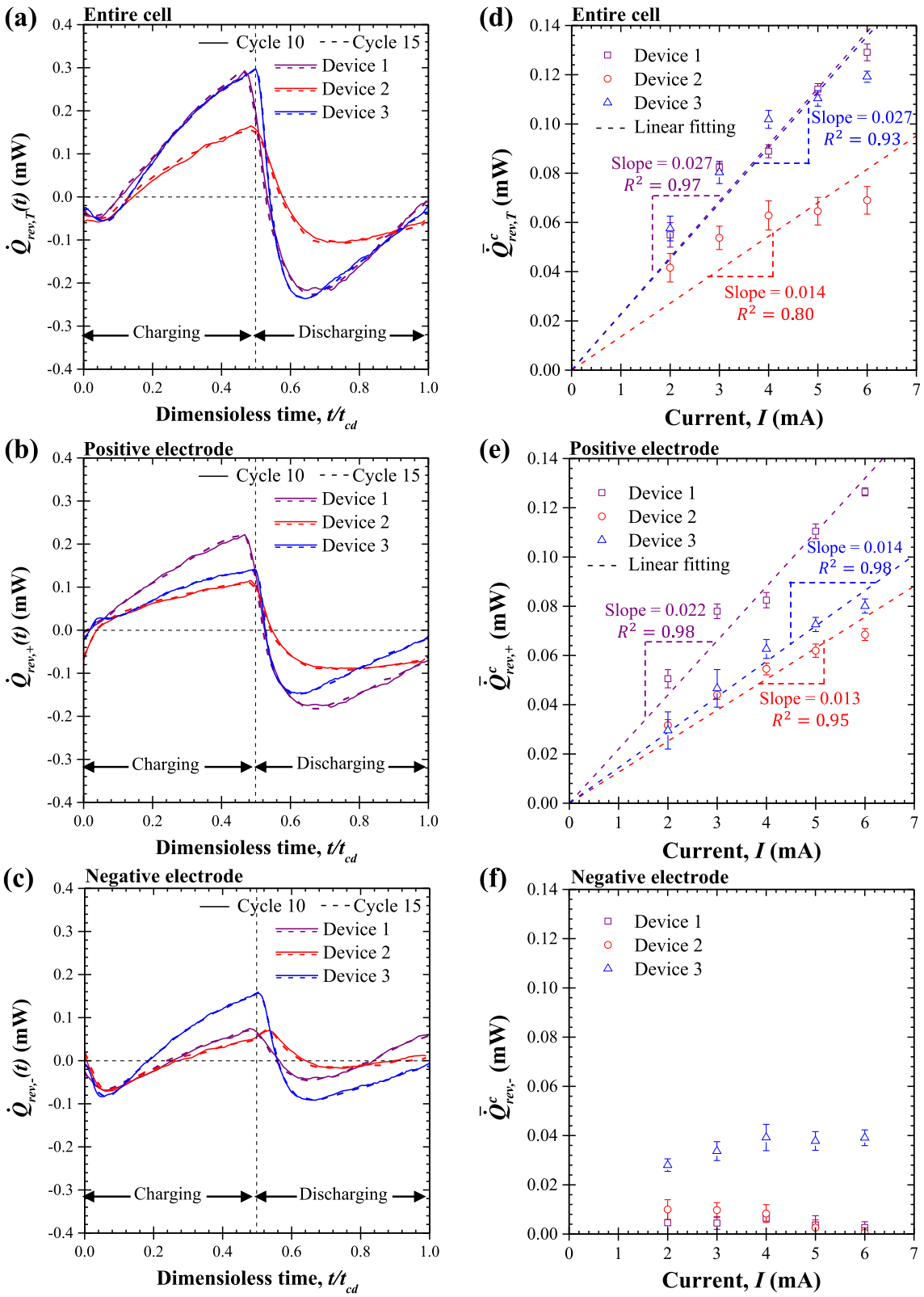

Fig. 7. Reversible heat generation rates (a) $\dot{Q}_{rev,T}(t)$ in the entire cell, (b) $\dot{Q}_{rev,+}(t)$ at the positive electrode, and (c) $\dot{Q}_{rev,-}(t)$ at the negative electrode as functions of the dimensionless time t/t_{cd} for two galvanostatic cycles under current I = 6 mA for Devices 1, 2, and 3. Time-averaged reversible heat generation rates during a charging step (d) $\bar{\dot{Q}}^{c}_{rev,T}$ in the entire cell, (e) $\bar{\dot{Q}}^{c}_{rev,+}$ at the positive electrode, and (f) $\bar{\dot{Q}}^{c}_{rev,-}$ at the negative electrode as functions of current I ranging between 2 and 6 mA for Devices 1, 2, and 3.

the charging or discharging steps. The reasons for this behavior remain unclear but could be associated with (i) parasitic reversible redox reactions involving the CMC binder, for example [42–44], (ii) reversible ion solvation/desolvation [45], and/or (iii) differences in ion size and/or diffusion coefficient in the electrolytes [17]. It is interesting to note that similar behavior has been observed theoretically at the pseudocapacitive electrode of hybrid capacitors [18].

Fig. 7 also shows the time-averaged reversible heat generation rates

during the charging step (d) $\bar{Q}^c_{rev,T}$ in the entire cell, (e) $\bar{Q}^c_{rev,+}$ at the positive electrode, and (f) $\bar{Q}^c_{rev,-}$ at the negative electrode as functions of current I ranging between 2 and 6 mA for the three EDLC devices considered (Table 1). Here, the reported values of $\bar{Q}^c_{rev,i}$ were the mean values of $\bar{Q}^c_{rev,i}$ obtained for 10 consecutive galvanostatic cycles and the error bars corresponded to two standard deviations or 95% confidence interval. The linear fit, obtained by least square method, is also shown to guide the eye. First, $\bar{Q}^c_{rev,T}$ ranged between 5 and 53% of the irreversible heat generation rate $\bar{Q}_T$ and decreased with increasing current. Interestingly, the time-averaged reversible heat generation rates $\bar{Q}^c_{rev,T}$ in the entire cell (Fig. 7(d)) and $\bar{Q}^c_{rev,+}$ at the positive electrode [Fig. 7(e)] were proportional to the current I for all devices. Such linear relationship has been previously observed experimentally [15] and predicted numerically [16]. By contrast, $\bar{Q}^c_{rev,-}$ at the negative electrode (Fig. 7(f)) was nearly constant and systematically lower than $\bar{Q}^c_{rev,+}$ at the positive electrode. In fact, it approached zero for Devices 1 and 2. This can be attributed to the fact that $\dot{Q}_{rev,-}(t)$ was endothermic in the early part of the charging step and exothermic only in the second part.

4.5. Effect of cell polarization

In order to confirm the differences in reversible heat generation rates observed between identical positive and negative electrodes the previous measurements were repeated with reverse cell polarity. In other words, each device consisted of Electrodes A and B. In the initial cell polarity, Electrodes A and B were the positive and negative electrodes, respectively. In this section, Electrode A was the negative electrode and Electrode B was the positive electrode.

Fig. 8(a) shows the time-averaged heat generation rates $\bar{Q}_+$ and $\bar{Q}_-$ at the positive and negative electrodes under galvanostatic cycling as functions of I^2 for current I ranging between 2 and 6 mA for the initial and the reverse cell polarities for Device 1, as illustrated in inset. As expected, Fig. 8(a) indicates that the time-averaged irreversible heat generation rates $\bar{Q}_i$ at Electrodes A and B remained unchanged under different polarizations. Slight deviations in $\bar{Q}_i$ between Electrode A and Electrode B for the two cell polarizations were due to minor differences in their resistances.

Similarly, Fig. 8(b) shows the time-averaged reversible heat generation rates $\bar{Q}^c_{rev,+}$ and $\bar{Q}^c_{rev,-}$ averaged during a charging cycle at Electrodes A and B of Device 1 as functions of current I ranging between 2 and 6 mA for the initial and reverse cell polarities. Here, the reversible heat generation rate $\bar{Q}^c_{rev,+}$ at the positive electrode was always positive and proportional to the current I. In other words, the time-averaged reversible heat generation rate $\bar{Q}^c_{rev,+}$ was unchanged when electrodes A or B served as the positive electrode and despite slight differences in the electrodes (e.g., resistance). Similarly at the negative electrode, $\bar{Q}^c_{rev,-}$ was nearly constant, relatively small, and unchanged regardless whether the negative electrode was Electrode A or B. Finally, note that the same results and observations were obtained with Devices 2 and 3 (see Supplementary Materials).

5. Conclusion

The present study designed, assembled, and carefully validated an isothermal calorimeter to investigate the temporal evolution of the heat generation rate in EDLC devices. This calorimeter was able to measure separately the instantaneous heat generation rates at each electrode of a two-electrode device with resolution as low as 10 μW and uncertainty of 3%. Heat generation measurements were demonstrated on three EDLC devices consisting of two identical activated carbon electrodes and different organic and aqueous electrolytes under galvanostatic cycling. First, the three devices were characterized using (i) cyclic voltammetry to obtain the gravimetric capacitance and (ii) galvanostatic cycling under constant current I to obtain the total internal resistance. Second, the measured time-averaged irreversible heat generation rates at each electrode were similar and proportional to I^2. The total irreversible heat generation rates measured in the entire EDLC cell were in excellent agreement with predictions for Joule heating. Third, the reversible heat generation rate $\dot{Q}_{rev,i}(t)$ was significantly different at the positive and negative electrodes and was independent of cell polarity. At the positive electrode, $\dot{Q}_{rev,+}(t)$ was systematically exothermic during charging and endothermic during discharging. By contrast, the reversible heat generation rate $\dot{Q}_{rev,-}(t)$ at the negative electrode was both exothermic and endothermic during either charging or discharging. In addition, $\bar{Q}^c_{rev,+}$ at the positive electrode was proportional to the current I while $\bar{Q}^c_{rev,-}$ at the negative electrode was systematically lower than $\bar{Q}^c_{rev,+}$ at the positive electrode and independent of the current I. The difference in

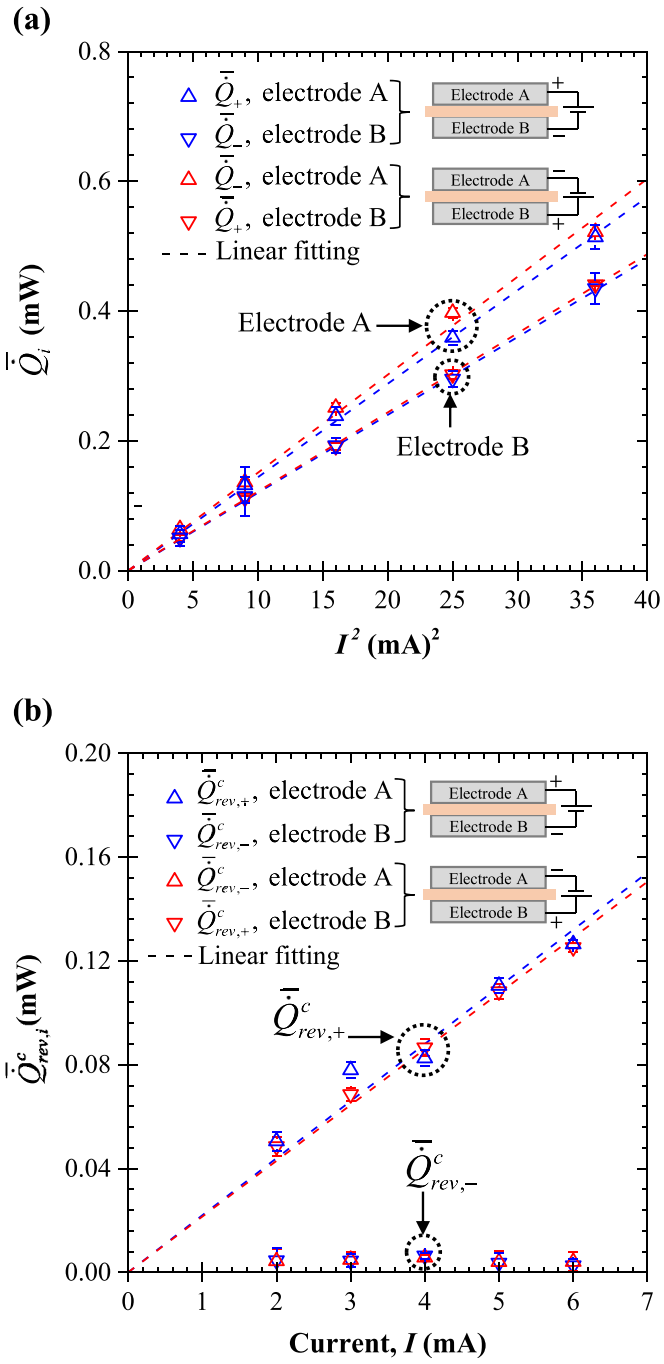

Fig. 8. (a) Irreversible heat generation rate $\bar{Q}_i$ and (b) time-averaged reversible heat generation rate $\bar{Q}^c_{rev,i}$ over a charging step at Electrodes A and B for Device 1 under galvanostatic cycling as functions of I^2 and I, respectively, for current I ranging between 2 and 6 mA for the initial and reverse EDLC cell polarities.

thermal behavior at the positive and negative electrodes may be due to parasitic reversible redox reactions, solvation/desolvation, and/or differences in ion size and transport properties in the electrolytes. Unfortunately, understanding the causes of such differences falls outside the scope of the present study but will be the subject of future research. Finally, the present results can be used to developed thermal management strategies for EDLCs. The isothermal calorimeter assembled could be used for other electrical energy storage systems and to gain insight into physicochemical phenomena taking place during charging and discharging.

Acknowledgment

O.M. is grateful for the financial support provided by King Fahd University of Petroleum and Minerals, Dhahran, Saudi Arabia. J.L. and B.D. were supported by the Office of Naval Research (under Grant N00014-16-1-2164).

Appendix A. Supplementary data

Supplementary data related to this article can be found at http://dx.doi.org/10.1016/j.jpowsour.2017.11.012.

References

[1] US Department of Energy, Basic Research Needs for Electrical Energy Storage: Report of the Basic Energy Sciences Workshop for Electrical Energy Storage. Tech. Rep. Office of Basic Energy Sciences, DOE, 2007, http://www.osti.gov/accomplishments/documents/fullText/ACC0330.pdf.
[2] B. Conway, Electrochemical Supercapacitors: Scientific Fundamentals and Technological Applications, Kluwer Academic/Plenum, New York, NY, 1999.
[3] P. Guillemet, Y. Scudeller, T. Brousse, Multi-level reduced-order thermal modeling of electrochemical capacitors, J. Power Sources 157 (1) (2006) 630–640.
[4] J. Miller, Electrochemical capacitor thermal management issues at high-rate cycling, Electrochimica Acta 52 (4) (2006) 1703–1708.
[5] A. Burke, Ultracapacitors: why, how, and where is the technology, J. Power Sources 91 (1) (2000) 37–50.
[6] A. Burke, R&D considerations for the performance and application of electrochemical capacitors, Electrochimica Acta 53 (3) (2007) 1083–1091.
[7] J. Miller, A. Burke, Electrochemical capacitors: challenges and opportunities for real-world applications, Electrochem. Soc. Interface 17 (2008) 53–57.
[8] J. Schiffer, D. Linzen, D.U. Sauer, Heat generation in double layer capacitors, J. Power Sources 160 (1) (2006) 765–772.
[9] H. Gualous, H. Louahlia-Gualous, R. Gallay, A. Miraoui, Supercapacitor thermal modeling and characterization in transient state for industrial applications, IEEE Trans. Industry Appl. 45 (3) (2009) 1035–1044.
[10] M. Al Sakka, H. Gualous, J.V. Mierlo, H. Culcu, Thermal modeling and heat management of supercapacitor modules for vehicle applications, J. Power Sources 194 (2) (2009) 581–587.
[11] O. Bohlen, J. Kowal, D. Sauer, Ageing behaviour of electrochemical double layer capacitors: Part II. lifetime simulation model for dynamic applications, J. Power Sources 173 (1) (2007) 626–632.
[12] C. Masarapu, H. Zeng, K. Hung, B. Wei, Effect of temperature on the capacitance of carbon nanotube supercapacitors, ACS Nano 3 (8) (2009) 2199–2206.
[13] D. Dunn, J. Newman, Predictions of specific energies and specific powers of double-layer capacitors using a simplified model, J. Electrochem. Soc. 147 (3) (2000) 820–830.
[14] K. Thomas, J. Newman, Thermal modeling of porous insertion electrodes, J. Electrochem. Soc. 150 (2) (2003) A176–A192.
[15] Y. Dandeville, P. Guillemet, Y. Scudeller, O. Crosnier, L. Athouel, T. Brousse, Measuring time-dependent heat profiles of aqueous electrochemical capacitors under cycling, Thermochim. Acta 526 (2011) 1–8.
[16] A.L. d'Entremont, L. Pilon, First-principles thermal modeling of electric double layer capacitors under constant-current cycling, J. Power Sources 246 (2014) 887–898.
[17] A.L. d'Entremont, L. Pilon, Thermal effects of asymmetric electrolytes in electric double layer capacitors, J. Power Sources 273 (2015) 196–209.
[18] A.L. d'Entremont, L. Pilon, First-principles thermal modeling of hybrid pseudocapacitors under galvanostatic cycling, J. Power Sources 335 (2016) 172–188.
[19] H. Gualous, H. Louahlia, R. Gallay, Supercapacitor characterization and thermal modelling with reversible and irreversible heat effect, IEEE Trans. Power Electron. 26 (11) (2011) 3402–3409.
[20] S. Al Hallaj, R. Venkatachalapathy, J. Prakash, J. Selman, Entropy changes due to structural transformation in the graphite anode and phase change of the $LiCoO_2$ cathode, J. Electrochem. Soc. 147 (7) (2000) 2432–2436.
[21] Y. Saito, K. Kanari, K. Takano, T. Masuda, A calorimetric study on a cylindrical type lithium secondary battery by using a twin-type heat conduction calorimeter, Thermochim. Acta 296 (1) (1997) 75–85.
[22] Y. Saito, K. Kanari, K. Takano, Thermal studies of a lithium-ion battery, J. Power Sources 68 (2) (1997) 451–454.
[23] H. Bang, H. Yang, Y. Sun, J. Prakash, In situ studies of $LixMn_2O_4$ and $LixAl_{0.17}Mn_{1.83}O_{3.97}S_{0.03}$ cathode by IMC, J. Electrochem. Soc. 152 (2) (2005) A421–A428.
[24] J. Kim, J. Prakash, J. Selman, Thermal characteristics of $Li_xMn_2O_4$ spinel, Electrochem. Solid-State Lett. 4 (9) (2001) A141–A144.
[25] W. Lu, J. Prakash, In situ measurements of heat generation in a Li/mesocarbon microbead half-cell, J. Electrochem. Soc. 150 (3) (2003) A262–A266.
[26] T. Bandhauer, S. Garimella, T. Fuller, A critical review of thermal issues in lithium-ion batteries, J. Electrochem. Soc. 158 (3) (2011) R1–R24.
[27] C. Pascot, Y. Dandeville, Y. Scudeller, P. Guillemet, T. Brousse, Calorimetric measurement of the heat generated by a double-layer capacitor cell under cycling, Thermochim. Acta 510 (12) (2010) 53–60.
[28] J. Hong, H. Maleki, S. Al Hallaj, L. Redey, J. Selman, Electrochemical-calorimetric studies of lithium-ion cells, J. Electrochem. Soc. 145 (5) (1998) 1489–1501.
[29] greenTEG, gSKIN Heat Flux Sensors for R&D: Instruction Manual, (2016) https://shop.greenteg.com/wp-content/uploads/gSKIN_Heat-Flux-Sensors-RD_Instructions_v1.7.pdf.
[30] E. Schwyter, T. Helbling, W. Glatz, C. Hierold, Fully automated measurement setup for non-destructive characterization of thermoelectric materials near room temperature, Rev. Sci. Instrum. 83 (7) (2012) 074904.
[31] R. Kamatchi, S. Venkatachalapathy, B. Srinivas, Synthesis, stability, transport properties, and surface wettability of reduced graphene oxide/water nanofluids, Int. J. Therm. Sci. 97 (2015) 17–25.
[32] K. Gadkaree, J. Liu, Microporous activated carbon for EDLCs, (July 9, 2013) US Patent 8,482,901.
[33] C. Yaws, Handbook of Thermal Conductivity vol. 3, Gulf Professional Publishing, Houston, TX, 1995.
[34] X. Jin, J. Wu, Z. Liu, J. Pan, The thermal conductivity of dimethyl carbonate in the liquid phase, Fluid Phase Equilibria 220 (1) (2004) 37–40.
[35] R. Hulse, M. Anderson, M. Bybee, D. Gonda, C. Miller, J. Oscarson, R. Rowley, W. Wilding, Liquid Thermal conductivities of acetonitrile, diethyl sulfide, hexamethyleneimine, tetrahydrothiophene, and tetramethylethylenediamine, J. Chem. Eng. Data 49 (5) (2004) 1433–1435.
[36] L. Pilon, H. Wang, A.L. d'Entremont, Recent advances in continuum modeling of interfacial and transport phenomena in electric double layer capacitors, J. Electrochem. Soc. 162 (5) (2015) A5158–A5178.
[37] A. Burke, M. Miller, Testing of electrochemical capacitors: capacitance, resistance, energy density, and power capability, Electrochimica Acta 55 (25) (2010) 7538–7548.
[38] S. Zhao, F. Wu, L. Yang, L. Gao, A. Burke, A measurement method for determination of dc internal resistance of batteries and supercapacitors, Electrochem. Commun. 12 (2) (2010) 242–245.
[39] M. Stoller, R. Ruoff, Best practice methods for determining an electrode material's performance for ultracapacitors, Energy & Environ. Sci. 3 (9) (2010) 1294–1301.
[40] J. Kotz, P. Treichel, J. Townsend, Chemistry and Chemical Reactivity, Cengage Learning, Belmont, CA, 2012.
[41] P. Kelter, M. Mosher, A. Scott, Chemistry: the Practical Science vol. 10, Cengage Learning, Boston, MA, 2008.
[42] L. Qiu, Z. Shao, D. Wang, F. Wang, W. Wang, J. Wang, Novel polymer Li-ion binder carboxymethyl cellulose derivative enhanced electrochemical performance for Li-ion batteries, Carbohydr. Polym. 112 (2014) 532–538.
[43] J. Drofenik, M. Gaberscek, R. Dominko, F. Poulsen, M. Mogensen, S. Pejovnik, J. Jamnik, Cellulose as a binding material in graphitic anodes for Li ion batteries: a performance and degradation study, Electrochimica Acta 48 (7) (2003) 883–889.
[44] L. Qiu, Z. Shao, M. Yang, W. Wang, F. Wang, J. Wan, J. Wang, H. Duan, Study on effects of carboxymethyl cellulose lithium (CMC-Li) synthesis and electrospinning on high-rate lithium ion batteries, Cellulose 21 (1) (2014) 615–626.
[45] M. Takeuchi, N. Matubayasi, Y. Kameda, B. Minofar, S. Ishiguro, Y. Umebayashi, Free-energy and structural analysis of ion solvation and contact ion-pair formation of Li^+ with BF_4^- and PF_6^- in water and carbonate solvents, J. Phys. Chem. B 116 (22) (2012) 6476–6487.